



Repositorio Institucional de la Universidad Autónoma de Madrid

<https://repositorio.uam.es>

Esta es la **versión de autor** del artículo publicado en:

This is an **author produced version** of a paper published in:

Journal of The Electrochemical Society 165.11 (2018): H688-H697

DOI: <https://doi.org/10.1149/2.1401810jes>

Copyright: © 2018 The Electrochemical Society

Access to the published version may require subscription
El acceso a la versión del editor puede requerir la suscripción del recurso

Design, construction and evaluation of a 3D printed electrochemical flow cell for the synthesis of magnetite nanoparticles.

I. Lozano^{1, 2}, C. López^{1, 2}, N. Menendez², N. Casillas³, P. Herrasti^{2*}

¹Departamento de Ingeniería Química, Universidad de Guadalajara, Centro Universitario de Ciencias Exactas e Ingenierías (CUCEI), Guadalajara, Jalisco, México.

²Departamento de Química Física Aplicada, Facultad de Ciencias, Universidad Autónoma de Madrid, Madrid, Spain.

³Departamento de Química, Universidad de Guadalajara, Centro Universitario de Ciencias Exactas e Ingenierías (CUCEI), Guadalajara, Jalisco, México.

*Corresponding author: email: pilar.herrasti@uam.es

Abstract

A 3D-printed prototype of an electrochemical flow cell for the synthesis of superparamagnetic magnetite nanoparticles of medium size between 15 and 30 nm was constructed and its performance was evaluated. The cell consists of a series of rectangular channels in a parallel electrode arrangement. Electrolyte flows through the channels as the electric current is supplied to the system and a combination of electrochemical and chemical reactions create the appropriate conditions for magnetite precipitation. Different electric configurations were evaluated and both energy and production efficiencies were calculated to determine the best configuration. Different flow and current values were also investigated, and all the materials were analyzed by X-ray diffraction, transmission electron microscopy, Mössbauer spectroscopy and magnetization curve measurements to determine their effect on particle morphology, composition and magnetic behavior. The best results were obtained for a parallel monopolar configuration, with 100 mA (3 mA cm^{-2}) passing in each two electrodes and a flow value of 30 mL min^{-1} , yielding an energy efficiency of 5.9 kJ g^{-1} and a production rate of 12.1 mg min^{-1} , approximately 6 times higher than the 100

mL standard cell previously used. Magnetic saturation was 77.3 emu g^{-1} , slightly lower than the bulk material ($92\text{-}100 \text{ emu g}^{-1}$).

Key words: Magnetite, Electrosynthesis, 3D printing, continuous flow cell

1. Introduction

Magnetite nanoparticles (MNPs) have become the subject of intense research in the last few years due to their wide variety of potential applications¹⁻⁴. Several techniques for the synthesis of this material are widely available, including: chemical precipitation⁵, a sol-gel process⁶, flame spray pyrolysis⁷, bacterial fermentation⁸ and electrochemical processes⁹⁻¹¹. Within this rapidly growing group of techniques, the electrochemical route offers several advantages that make it attractive for specific applications. For example, electrochemical processes can produce a clean product with a well-controlled nanoparticle size, on the order of 20 to 30 nm, and narrow size distribution with excellent magnetic properties convenient for some biomedical applications, such as hyperthermia^{10,12}.

Electrochemical synthesis of MNPs applies a controlled current (or potential) between two iron electrodes submerged in an electrolyte. Iron electrochemical dissolution (equation 1) is the main reaction that occurs on the anode and water reduction is the most prominent on the cathode (equation 2). The pH value rises due to OH^- production on the cathode, and Fe^{2+} species generated at the anode can react to form $\text{Fe}(\text{OH})_2$ (equation 3) that can be oxidized in the presence of dissolved oxygen in the electrolyte (equation 4), to form $\gamma\text{-FeOOH}$ (lepidocrocite). Then, these oxyhydroxide species undergo a topotactic transformation (catalysed by Fe^{2+}) to produce magnetite (equation 5)¹³⁻¹⁵.

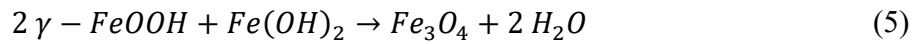
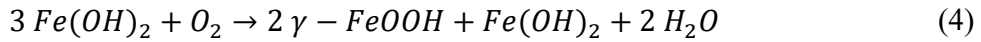
Anode:



Cathode:



In solution:



One of the main drawbacks of electrochemical synthesis of MNPs is the low yield values for laboratory-scale synthesis (1.9 mg min⁻¹ in a standard batch synthesis¹⁵). Briefly, the standard batch electrosynthesis is carried out in a cell (100 mL), and two iron electrodes as cathode (8 cm²) and anode (2 cm²) are used. The production rate is directly controlled by the current supplied to the electrochemical media however, increasing yield while maintaining the same morphology and structural characteristics is not a straight forward task. There are several approaches for scaling up production, i.e., enlarging the size and number of electrodes, increasing current density or increasing synthesis time. In this paper, we use a combination of all of these approaches by employing a parallel electrode flow cell inspired by designs used for waste water electrocoagulation treatment due to the similarities shared by both of these processes^{16,17}.

The construction of a working prototype can be an expensive and time-consuming endeavor however, 3D printing has recently become an accessible and low-cost alternative for fast lab-scale prototyping, allowing for the production of complex designs that would otherwise require expensive manufacturing processes^{18–23}. The 3D printing process begins by creating a virtual model of the desired geometry. This can be accomplished using a variety of techniques, i.e. computer aided design (CAD) software, 3D scanners or photogrammetry. The model can then be “sliced”, which consists in the generation of several 2D cross section layers that describe the geometry entirety. The result of the slicing process is a coordinates file that the printer can use to deposit layers of material one on top of the other until the desired 3D object is created. There are 4 main categories of 3D printing technologies: extrusion, powder-based, lamination and photopolymerization. The most common technique by far is extrusion, specifically, fused deposition modelling (FDM), which uses thermoplastic materials such as polylactic acid (PLA), acrylonitrile butadiene styrene (ABS), polycarbonate (PC) and polyamide (PA)²⁴. Through combining 3D printing with finite element modelling (FEM), it is possible to create a very robust prototyping system that allows identification of possible improvement opportunities.

Additive manufacturing has proven its usefulness in electrochemical applications such as conductive polymer-based 3D models²⁵, electrochemical flow cells^{22,26}, redox flow batteries²³, biosensors^{27–29} and 3D-printed reaction and fluidic systems^{29,30}.

The objective of this study is to evaluate the performance of a flow cell constructed through 3D printing for producing magnetite nanoparticles and increasing the yield without changing their magnetic and structural properties.

2. Experimental

2.1 Electrochemical cell design and construction

The cell was first conceived using the 3D modelling computer software SketchUp, to create a *.stl-format file that was then sliced using the 3D print preparation software Cura® for the creation of a G-code file suitable for input into most 3D printing hardware³¹. The entire object was constructed out of PLA using an Ultimaker 2® 3D printer with a 0.4 mm nozzle size and a 0.06 mm layer height. The cell's main body is comprised of a series of chambers that allow electrolyte to move in a plug flow fashion. The electrodes and top cover are also part of the geometry and help to define the channels through which the electrolyte can flow.

The cell features an inlet flow manifold is shown in Figure 1A, which is comprised of a series of channels that distribute the main inlet flow and supplies it to the first electrode chamber, when the chamber floods, it spills over the top edge of the electrode and into the adjacent chamber, this process is repeated until the main and only outlet is reached. The clearance between the top edge of the electrodes and the cover of the cell had originally a value of 1 cm, however, we noticed some minor leaking due to an excess of foam caused by intense bubbling (equation 2) and decided to increase this value to 3 cm for all experiments reported here. The flow manifold allows a more homogeneous distribution of the electrolyte flow along the electrodes entire length.

The 8 plates (100 mm x 45 mm) that were used as electrodes were machined out of low carbon steel sheets of 1 mm thickness and 99.8% wt. iron purity. A small 5 mm section protruded from the edge of each of the electrodes to use as an electrical connection and a

10-mm separation was kept between electrodes in all chambers (Figure 1B). We selected a 10 mm separation as an optimum value based on a previous study conducted by the research group¹¹. A photo of a finished prototype is shown in Figure 1C.

A 1 g L⁻¹ solution of NaCl acquired from PANREAC (above 99% purity), was used as a supporting electrolyte. The water employed for all solutions was treated to a conductivity of 0.1 $\mu\text{S cm}^{-1}$ in an Ecomatic deionizing equipment by Wasserlab. The electrolyte was supplied to the cell using a Heidolph Pumpdrive 5201 peristaltic pump operating at 30 mL min⁻¹, and the cell's total volume was 460 mL.

Direct current was supplied using a Dosban Industrial AFX3333C DC power supply and a multimeter connected in series to confirm the total current value. To assess the effect of the electrical configuration on the electrosynthesis, two different electric combinations were tested: bipolar electrodes in series connection (BP-S), and monopolar electrodes in parallel connection (MP-P). In the first configuration the total current applied was 100 mA (3 mA cm⁻²). In the second connection a total current of 700 mA was applied, so the current through each cell was also 100 mA (3 mA cm⁻²), considering that the resistance into each cell was the same (see FEM simulation). A schematic representation of the two different configurations is shown in Figure 2.

A Crison basic 20 pH-meter and probe was employed for pH value recording at the outlet flow cell. The nanoparticles were collected with a neodymium magnet placed on the bottom of the beaker. The solutions were discarded and the nanoparticles were washed several times and collected every time with the magnet. Afterwards, the nanoparticles were dried in a vacuum system over night.

2.2 FEM simulations

The hydrodynamic behavior and electrical configuration were modeled by FEM simulation. The first part of the simulation was computed using the laminar flow module in COMSOL®. Equations 6 and 7 were solved for incompressible flow in the stationary state, considering no slip boundaries for static walls, laminar flow boundaries for electrolyte inlet and outlet and moving wall boundaries for simulation of H₂ bubbling on the surfaces of the cathodes and O₂ on the anodes. A summary of the boundary conditions and parameters employed is presented in Table 1.

$$\rho(\mathbf{u} \cdot \nabla)\mathbf{u} = \nabla \cdot [-p\mathbf{I} + \mu(\nabla\mathbf{u} + (\nabla\mathbf{u})^T)] + \mathbf{F} \quad (6)$$

$$\rho\nabla \cdot (\mathbf{u}) = 0 \quad (7)$$

where: \mathbf{u} = velocity field; p = pressure; ρ = fluid density (water at 25 °C); μ = fluid viscosity (water at 25 °C); \mathbf{I} is the identity matrix, T denotes the transpose operation and \mathbf{F} represents the external forces applied to the fluid and \mathbf{n} is the normal vector.

The second part of the FEM simulation was carried out using COMSOL's secondary current distribution module to analyse the potential and current distribution in the electrodes and electrolyte. The module solves the current distribution in the electrolyte according to Ohm's law. The kinetics of the electrodes were described by the Butler-Volmer expression in addition to the dissolution resistance. The conductivity of the supporting electrolyte (NaCl) was 0.199 S.m⁻¹. The electrochemical reactions considered at the surface of the electrodes were the oxidation of iron at the anode and the reduction of water at the cathode, according with the observed mechanism¹⁵. The different electric

configurations were simulated by changing the position of the electrode current boundary. A summary of the parameters and boundary conditions used in the simulations is presented in Table 2, where: \mathbf{i}_s denotes the current density vector in the electrode (\mathbf{i}_l for the electrolyte), σ_s denotes the conductivity, ϕ_s the electric potential in the metallic conductor (ϕ_l for electrolyte potential), and Q_s denotes a general current source term (usually zero).

2.3 Sample characterization parameters

Before any characterization, the electrosynthesized material was washed several time collected with a magnet and dry in a vacuum oven.

The morphology of the synthesized nanoparticles was investigated by means of transmission electron microscopy (TEM). Micrographs of the synthesized nanoparticles were collected in a JEOL JEM 1010 instrument operating at an acceleration voltage of 100 kV. The average size of the nanoparticles is calculated by measuring at least 100 nanoparticles, analyzing their distribution. The crystalline phase and the crystal size of the resulting nanoparticles were investigated by X-ray diffraction (XRD). X-ray diffractograms were recorded between 10° and 80° 2θ in a D5000 diffractometer equipped with a secondary monochromator and SOL-X Bruker detector with Cu K α radiation and analysed using the FullProf Suite program³² based on the Rietveld refinement method. Magnetic characterization was carried out using a vibrating sample magnetometer (MLVSM9 MagLab 9T, Oxford instruments). The magnetization curves were measured at room temperature after applying a maximum magnetic field of 3 T. Parameters such as the saturation magnetization (Ms) and the coercive field (Hc) were derived from the magnetization curves.

Mössbauer spectra were registered at room temperature and at 77 K in a triangular mode using a conventional spectrometer with a $^{57}\text{Co}(\text{Rh})$ source. The spectral analyses were performed with a non-linear adjustment, using the NORMOS program³³. The calibration energy was performed with an $\alpha\text{-Fe}$ (6 μm) foil.

3. Results and Discussion

Figure 3 shows the FEM simulation of the flow speed distribution for the inlet flow manifold and the lateral view of the cell's main body. It can be observed that the flow diffuser was able to distribute the flow velocity evenly at the entrance to the main cell body. The average flow speed value obtained from the geometry's outlet boundaries on Figure 3A was $0.27 \pm 0.02 \text{ cm s}^{-1}$, which was then employed as the inlet flow speed value for the simulation in the main body (Figure 3B). According to the results, the inlet flow manifold can create a homogeneous flow speed distribution along the electrode length. Additionally, the main body flow speed distribution did not show any major stagnation zone. The flow was characterized as laminar ($Re < 2100$) throughout the main body of the cell.

Figure 4A shows the results of the electrolyte potential distribution for the MP-S configuration. The electrolyte potential diminishes (from approximately 12 to 2 V) as the distance from the electrode connected to the power supply is increased. The arrows show the direction of the current flow in the electrolyte. When compared with the parallel configuration (Figure 4B), the arrows indicate that the current does not travel in the same direction across all of the cell instead, it travels from the positive surfaces (anodes) to the

negative surfaces (cathodes). Potential values for the parallel configuration are lower, as expected, when compared with the series configuration.

The current density distribution in the electrodes helps us to better visualize high-current density zones, which are directly related to the distribution of reactive species throughout the cell. The current density distribution for the series configuration (Figure 4C) shows that the current density profiles in every electrode are different and that most of the current is concentrated in the outer electrodes, in agreement with the potential simulation. This behavior was also observed during experimentation. When the electrodes were taken out of the cell, it was clear that the outer anodes had suffered a drastically higher loss of material than had the inner anodes.

On the other hand, the electrode current density distribution in the parallel configuration (Figure 4D) shows a gradient in the vertical direction in each electrode, however, this distribution is the same in all inner electrodes which suggests a more homogeneous current distribution along the cell when compared with that of the series configuration. It is noteworthy to mention that the material lost in all anodes was visually similar for the parallel configuration.

3.1 Cell performance

To evaluate the behavior and efficiency of the flow cell in the two electrical configurations tested, the cell total voltage and the pH value of the outlet solution were recorded (Figure 5).

As seen in Figure 5A, the cell voltage diminished from 15 to 12 V for BP-S and from 2.5 to 1.5 V for MP-P during the first minutes of synthesis. This is due to the increment in electrolyte conductivity, which is a direct result of the production of ionic species. Voltage values remained relatively constant ($\Delta V/\text{min} < 0.01 \text{ V/min}$) after 10 minutes for the MP-P configuration and after 30 minutes for BP-S. A sudden increase in pH values was recorded during the first few minutes of synthesis for both configurations (Figure 5B), and maximum (11.5 for BP-S and 12.5 for MP-P) was reached around the 10-minute mark. After that, pH values steadily decrease, but remained above 10. The pH evolution is of special relevance because hydroxylated compounds of iron act as a precursor species for the electrochemical formation of magnetite¹⁵.

Energy consumption (EC) was calculated using the total cell voltage data from Figure 5A between the initial ($t_i = 40 \text{ min}$) and final ($t_f = 70 \text{ min}$) collection times. The initial collection time was fixed at 40 min into the synthesis to ensure that the cell voltage was virtually constant. Efficiency was calculated by comparing the maximum obtainable Fe_3O_4 mass for the experimental parameters used, with the real production rate (PR), after several washes. Results are shown in Table 3. This table shows a comparison of the efficiency of both series and parallel configurations for 30 min. of synthesis, in both cases between 40 and 70 min. of the overall process (once a constant voltage is reached)

These results show that the best performance (highest efficiency and production rate) was obtained when working with an MP-P configuration. Given that efficiency is an indirect measure of the system's ability to transform Fe^{2+} into magnetite¹⁵, lower efficiency values, as found for BP-S, could indicate the formation of secondary species, which are removed during successive washing and rinsing processes and collected with a magnet. The

ability to transform Fe^{2+} into magnetite is strongly influenced by the distribution of the reactive species in the medium. In electrocoagulation systems for water treatment, MP-P configurations have been also found to be the most efficient³⁴ due to their better current distribution between electrodes and the fact that pollutant removal efficiency, for electrocoagulation processes, is directly influenced by the production uniformity of the dissolving metal¹⁶. These results also support the current distributions shown in the FEM simulations and the known relation between a homogeneous current distribution and better cell performance.

3.2 Sample characterization in the different configurations

Figure 6 shows a comparison of micrographs taken of samples obtained from the different electric configurations studied. The nanoparticles displayed a quasi-spherical morphology in all cases. The mean particle diameter was calculated from at least 100 direct measurements. Nanoparticles with a mean diameter of 30 ± 2 nm were measured for the MP-P configuration sample, which are of a very similar size than the ones obtained in the standard batch synthesis (25-33 nm)¹¹. For the BP-S configuration, the mean diameter was found to be 20 ± 1 nm. The arrows in Figure 6 A indicate the presence of a secondary species. For MP-P, the presence of secondary phases was negligible, and the nanoparticles obtained were larger and better-defined than the ones obtained for the series arrangement.

Figure 7 shows the diffractograms obtained from samples collected from the two electric configurations studied. The typical diffraction peaks of magnetite can be observed (JCPDS 01-088-031). However, for the BP-S configurations, an additional peak at $2\theta = 40.5^\circ$ was recorded. This signal cannot be assigned to a spinel structure and indicates the presence of an oxyhydroxide secondary species such as $\alpha\text{-FeOOH}$ ³⁵ (JCPDS 81-0462).

Additionally, the Rietveld refinement method was applied to the XRD data to fit the crystal structure of the magnetite. Table 4 shows a summary of the parameters obtained from the Rietveld refinement method. The crystal size (16.6 and 21.1 nm for BP-S and MP-P respectively) was found to be smaller than the particle size measured from the TEM micrographs (20 and 30 nm for BP-S and MP-P respectively) because the particles were not monocrystalline. The lattice parameter calculated is very close (within a 1% deviation) to previous reports in the literature³⁶ for magnetite nanoparticles. No significant changes were detected related to the electrical configuration used. The agreement factors Rp and chi squared (χ^2) have acceptable values for this fitting.

Although goethite was detected by XRD in the material synthesized using the BP-S configurations, it is not possible to make a quantitative analysis of the products due to the small amount detected and to a certain amorphous character observed in the Mössbauer spectra (Figure 8). The Mössbauer spectra in all cases were fitted as the sum of different subspectra: two magnetic subspectra with hyperfine magnetic fields $H=48.5(3)\text{T}$ (isomer shift= $0.31(1)\text{ mm/s}$) and $H=45.0(2)\text{T}$ (isomer shift= $0.4(1)\text{ mm/s}$), corresponding to Fe^{3+} in the tetrahedral position and $[\text{Fe}^{3+}/\text{Fe}^{2+}]$ in octahedral coordination in the magnetite spinel structure, respectively. In addition to the two sextets, there is one doublet with isomer shift= $0.2(1)\text{ mm/s}$ and quadrupole splitting = $0.5(1)\text{ mm/s}$ that may be due to the presence of some non-magnetic Fe^{3+} oxide, oxyhydroxide or Fe_3O_4 itself with a particle size of less than $10\text{ nm}^{11,37}$. The effect of cooling to 77K (spectra not showed) shows up that the particle size is less than 10 nm , as the doublet was not observed at this temperature. In the samples obtained using the BP-S configurations, a third sextet was observed (green subspectrum in Figure 8A). In this case, due to the width of the peaks, the sextet has been interpreted as a

distribution of hyperfine magnetic fields with average parameters of $H = 40$ (2) T and $\delta = 0.37$ mm/s. Although the quantities of Fe assigned to the goethite by Mössbauer spectroscopy (30%) should be observed in the diffractograms, it is possible that we are overestimating the area of the subspectrum because it overlaps with the signal of the magnetite. In the MP-P sample, the hyperfine parameters confirm that the only species present is Fe_3O_4 .

Figure 9 shows a comparison of the magnetization curves recorded at room temperature for products obtained from both configurations. According to these results, the MP-P sample presents the highest magnetization saturation (77.3 emu/g). This was to be expected, given that the particle size follows the same trend. As the particle gets smaller, surface effects become more significant. Squareness (M_r/M_s) was found to decrease for smaller particles, and the coercivity was very close to superparamagnetic values, as expected for oxide nanoparticles whose size is below 20 nm. The decrease in magnetic saturation is a result of the combined effect of the smaller nanoparticle size and the presence of a paramagnetic phase ($\alpha\text{-FeOOH}$)³⁸ detected by TEM, XRD and Mössbauer spectroscopy. A summary of the parameters obtained from the magnetization curves is shown in Table 5.

3.4 Synthesis parameters evaluation for MP-P configuration

After determining MP-P as the best electrical configuration in the continuous flow synthesis, the effects of synthesis parameters on the properties of the nanoparticles were evaluated, starting with the study of the effect of variation of the electrolyte flow at the entrance of the cell maintaining a constant current of 100 mA (3 mA cm^{-2}).

The increase in flow did not modify significantly the Fe₃O₄ production rate. A yield of 12.1 mg min⁻¹ was obtained for the original flow of 30 mL min⁻¹. As flow increased to 60 and 90 mL min⁻¹, production rose to 12.3 and 13.2 mg min⁻¹, respectively. No secondary species appeared when the electrolyte flow was modified in this range, and the morphology of the Fe₃O₄ nanoparticles and the lattice parameters were preserved. However, the mean particle size measured by TEM (Figure 10) decreases with increasing flow rates (30 ± 2 nm with a flow of 30 mL min⁻¹, 20 ± 1 nm for 60 mL min⁻¹ and 15 ± 1 nm for 90 mL min⁻¹) due to the reduction in the residence time of the particles in the cell body which causes an interruption in the growth phase. This effect was also observed in the crystal size calculated in the Rietveld refinements which showed that for 30, 60 and 90 mL min⁻¹, the crystal sizes were 21.1, 17.8 and 15.6 nm respectively. It is noteworthy to mention that when using an electrolyte flow of 90 mL min⁻¹, the difference between the crystal size obtained from the Rietveld refinement (15.6 nm) and the particle size calculated from the TEM micrographs (15 nm) was virtually nonexistent, which suggests that monocrystalline particles with a lattice parameter of 8.332 Å can be obtained under these conditions.

The applied current variation on the MP-P flow cell was investigated under a constant flow of 30 ml min⁻¹ and it showed that neither the form nor the size of the Fe₃O₄ nanoparticles were modified. As applied current was increased, the production rate also rise, production grew from the original 12.1 ± 0.1 to 24.8 ± 0.2 and 47.5 ± 0.1 mg min⁻¹ for 200 and 300 mA respectively, however, the increase of current also favors goethite formation (Figure 11). Current density at the electrode surface is a relevant factor for the nucleation rate and is related to the production of both Fe²⁺ and OH⁻ (equation 1 and 2), but the production of magnetite becomes limited by the conversion of FeOOH to Fe₃O₄

(equation 5). Thus, an increment in the flow rate affects the growing stage, but not the nucleation processes. From the Rietveld refinements performed on the XRD diffractograms shown in Figure 12, it can be quantified that 21% of the synthesized product was α -FeOOH when the applied current was 200 mA and that this increased up to 29% when the current was 300 mA. The fact that the shape and size of the nanoparticles remained practically constant during variation of the current intensity indicates that this parameter affects the number of nuclei formed but does not affect the growth phase of the nanoparticles, although it promotes the formation of secondary species that decrease the purity of the synthesized material.

Since Fe_3O_4 formation is limited by the topotactic transformation process of oxyhydroxide species (FeOOH) in the presence of Fe^{2+} ionic species¹⁵, as the current in the system increases, an excess of Fe^{2+} species is likely to develop in the form of $\text{Fe}(\text{OH})_2$ due to the high pH conditions. This excess of hydroxylated species will be eventually oxidized by the oxygen dissolved in the medium without undergoing a topotactic transformation to Fe_3O_4 , which would explain the occurrence of a higher presence of oxyhydroxide species when the applied current was increased.

4. Conclusions

A new electrochemical flow cell was designed, built and its performance evaluated for the electrosynthesis of magnetite nanoparticles. The best electrochemical configuration, determined based on production rate and energetic efficiency, was MP-P, which probably provides a better current distribution along the cell's electrodes. Direct measurements from

TEM micrographs showed that for the MP-P configuration, the mean particle diameter decreased with increasing electrolyte flow, changing from 30 ± 2 nm for a 30 mL min^{-1} flow to 15 ± 1 nm for a 90 mL min^{-1} . The nanoparticles synthesized with the highest flow value were found to be monocrystalline. The crystal structure was confirmed by means of XRD, and an additional secondary phase (identified as $\alpha\text{-FeOOH}$) was found for the product of the series configurations and for the parallel configuration only when current was increased. Magnetic saturation was higher for the MP-P configuration due to the lack of a paramagnetic phase, with coercivity values close to a superparamagnetic behavior and in good agreement with previous literature reports. In terms of productivity, the prototype cell improved the production rate by a factor of approximately 6 compared with the standard batch synthesis¹⁵.

5. Acknowledgments

The authors gratefully acknowledge the scholarship for doctoral studies of Gerardo Ivan Lozano Gutierrez granted by the National Council of Science and Technology of Mexico (CONACyT). The authors are also grateful to the Ministry of Economy and Competitiveness for the project MAT2015-67557-C2-2-P. Support for a sabbatical leave for NCS from the National Council of Science and Technology of Mexico and Exportadora de Postes S.A. de C.V. are greatly appreciated.

6. References

1. R. Tietze et al., *Biochem. Biophys. Res. Commun.*, **468**, 463–470 (2015)
<http://dx.doi.org/10.1016/j.bbrc.2015.08.022>.
2. R. Kaur et al., *J. Sep. Sci.*, **37**, 1805–1825 (2014).
3. S. Genc and B. Derin, *Curr. Opin. Chem. Eng.*, **3**, 118–124 (2014)
<http://www.sciencedirect.com/science/article/pii/S2211339813001226>.
4. Á. León, M. Epifani, T. Chávez, J. Palma, and R. Díaz, *Int. J. Electrochem.*, **9**, 3837–3845 (2014).
5. S. A. Kahani and M. Jafari, *J. Magn. Magn. Mater.*, **321**, 1951–1954 (2009)
<http://www.sciencedirect.com/science/article/pii/S0304885308012766>.
6. O. Lemine et al., *Superlattices Microstruct.*, **52**, 793–799 (2012)
<http://www.sciencedirect.com/science/article/pii/S0749603612002042>.
7. R. Strobel and S. E. Pratsinis, *Adv. Powder Technol.*, **20**, 190–194 (2009)
<http://www.sciencedirect.com/science/article/pii/S0921883108000289>.
8. J.-W. Moon et al., *J. Ind. Microbiol. Biotechnol.*, **37**, 1023–1031 (2010)
<http://link.springer.com/article/10.1007/s10295-010-0749-y>.
9. C. Tsouris, D. W. DePaoli, J. T. Shor, M. C. Z. Hu, and T. Y. Ying, *Colloids Surfaces A Physicochem. Eng. Asp.*, **177**, 223–233 (2001).
10. T.-Y. Ying, S. Yiacoumi, and C. Tsouris, *J. Dispers. Sci. Technol.*, **23**, 569–576 (2002).
11. L. Cabrera, S. Gutierrez, N. Menendez, M. P. Morales, and P. Herrasti, *Electrochim.*

Acta, **53**, 3436–3441 (2008).

12. F. Fajaro, H. Setyawan, W. Widiyastuti, and S. Winardi, *Adv. Powder Technol.*, **23**, 328–333 (2012) <http://www.sciencedirect.com/science/article/pii/S092188311100063X>.

13. E. Tronc, P. Belleville, J. P. Jolivet, and J. Livage, *Langmuir*, **8**, 313–319 (1992).

14. Y. Tamaura, M. Saturno, K. Yamada, and T. Katsura, *Bull. Chem. Soc. Jpn.*, **57**, 2417–2421 (1984).

15. I. Lozano, N. Casillas, C. Ponce de León, F. C. Walsh, and P. Herrasti, *J. Electrochem. Soc.*, **164**, 184–191 (2017).

16. A. Vázquez, I. Rodríguez, and I. Lázaro, *Chem. Eng. J.*, **179**, 253–261 (2012) <http://dx.doi.org/10.1016/j.cej.2011.10.078>.

17. W. Ying-Chieh, I. A. Rusakova, A. Baikalov, J. W. Chen, and W. Nae-Lih, *J. Mater. Res.*, **20**, 75–80 (2005).

18. A. Matta, D. Raju, and K. Suman, *Mater. Today Proc.* (2015) <http://www.sciencedirect.com/science/article/pii/S2214785315005647>.

19. G. I. Peterson, M. B. Larsen, M. A. Ganter, D. W. Storti, and A. J. Boydston, *ACS Appl. Mater. Interfaces*, **7**, 577–583 (2015) <http://pubs.acs.org/doi/abs/10.1021/am506745m>.

20. I. T. Nassar, H. Tsang, K. Church, and T. M. Weller, in *IEEE Radio and Wireless Symposium, RWS*, p. 67–69 (2014) http://ieeexplore.ieee.org/xpls/abs_all.jsp?arnumber=6830137.

21. I. T. Nassar and T. M. Weller, in *BioWireless 2013 - Proceedings: 2013 IEEE Topical Conference on Biomedical Wireless Technologies, Networks, and Sensing Systems - 2013*

IEEE Radio and Wireless Week, RWW 2013, p. 85–87 (2013)

http://ieeexplore.ieee.org/xpls/abs_all.jsp?arnumber=6490199.

22. C. P. De Leon, W. Hussey, F. Frazao, D. Jones, and E. Ruggeri, *Chem. Eng. Trans.*, **41**, 1–6 (2014).

23. L. F. Arenas, F. C. Walsh, and C. P. de León, *ECS J. Solid State Sci. Technol.*, **4**, P3080–P3085 (2015) <http://jss.ecsdl.org/content/4/4/P3080.abstract>.

24. A. Ambrosi and M. Pumera, *Chem. Soc. Rev.*, **45** (2016)

<http://dx.doi.org/10.1039/C5CS00714C>.

25. X. Wei et al., *Sci. Rep.*, **5**, 11181 (2015)

<http://www.nature.com/articles/srep11181>
<http://www.nature.com/srep/2015/150708/srep11181/full/srep11181.html>.

26. M. E. Snowden, P. H. King, J. A. Covington, J. V. MacPherson, and P. R. Unwin, *Anal. Chem.*, **82**, 3124–3131 (2010).

27. L. Krejcová et al., *Biosens. Bioelectron.*, **54**, 421–427 (2014)

<http://dx.doi.org/10.1016/j.bios.2013.10.031>.

28. S. A. N. Gowers et al., *Anal. Chem.*, **87**, 7763–7770 (2015).

29. J. L. J. Erkal et al., *Lab Chip*, **14**, 2023–32 (2014)

<http://www.scopus.com/inward/record.url?eid=2-s2.0-84901022826&partnerID=tZOtx3y1>.

30. P. J. Kitson, M. H. Rosnes, V. Sans, V. Dragone, and L. Cronin, *Lab Chip*, **12**, 3267 (2012).

31. B. Berman, *Bus. Horiz.*, **55**, 155–162 (2012)

<http://dx.doi.org/10.1016/j.bushor.2011.11.003>.

32. J. Rodríguez-Carvajal, *Phys. B Condens. Matter*, **192**, 55–69 (1993).

33. R. A. Brand, *Nucl. Instruments Methods Phys. Res. Sect. B Beam Interact. with Mater. Atoms*, **28**, 398–416 (1987).

34. Y. Demirci, L. C. Pekel, and M. Alpbaz, *Int. J. Electrochem. Sci.*, **10**, 2685–2693 (2015).

35. E. Mazarío, P. Herrasti, M. P. Morales, and N. Menéndez, *Nanotechnology*, **23**, 355708 (2012) <http://iopscience.iop.org/0957-4484/23/35/355708>.

36. H. E. Swanson, N. T. Gilfrich, and G. M. Ugrinic, *U.S. Gov. Print. Off. Circ. Natl. Bur. Stand. 539*, **25**, 26 (1955).

37. E. Mazario, M. P. Morales, R. Galindo, P. Herrasti, and N. Menendez, *J. Alloys Compd.*, **536**, S222–S225 (2012) <http://dx.doi.org/10.1016/j.jallcom.2011.10.073>.

38. A. M. Hirt, L. Lanci, J. Dobson, P. Weidler, and A. U. Gehring, *J. Geophys. Res.*, **107**, doi:10.1029/2001JB000242 (2002) <http://doi.wiley.com/10.1029/2001JB000242>.

FIGURE CAPTION

Figure 1. 3D printed electrochemical scheme. A) Expanded view with top cover and electrodes halfway in. B) Main body cross section view (not to scale). C) Photo of the finished prototype.

Figure 2. Electrical configurations for the electrochemical flow cell: A) In series bipolar, BP-S and B) Parallel monopolar, MP-P.

Figure 3. FEM simulated stationary flow speed (cm s^{-1}) distribution for A) Inlet flow manifold and B) main cell's body.

Figure 4. FEM simulated electric potential distribution in the electrolyte for: A) Series bipolar and B) Parallel monopolar configurations. Dimensionless electrode current density distribution for: C) Series bipolar and D) Parallel monopolar configurations.

Figure 5. A) Flow electrochemical cell voltage, and B) exit pH value, during electrosynthesis at 30 mL min^{-1} electrolyte flow and current density of 3 mA cm^{-2} .

Figure 6. TEM micrographs and size distribution histogram of Fe_3O_4 nanoparticles obtained for A) BP-S, and B) MP-P configurations. Nanoparticles obtained at 30 mL min^{-1} electrolyte flow and 3 mA cm^{-2} current density. The arrows in A) indicate the presence of $\alpha\text{-FeOOH}$ as secondary species.

Figure 7. Magnetite nanoparticles XRD diffractogram comparison for the material obtained for two different electric configurations, at 30 mL min^{-1} electrolyte flow and 3 mA cm^{-2} current density.

Figure 8. Magnetite nanoparticles Mössbauer spectra at room temperature. Fe_3O_4 obtained for A) BP-S and B) MP-P configurations, both at 30 mL min^{-1} electrolyte flow and 3 mA cm^{-2} current density. The green line in A) indicate the presence of $\alpha\text{-FeOOH}$ as secondary species.

Figure 9. Hysteresis measurements, recorded at 300K, of Fe_3O_4 nanoparticles obtained at 30 mL min^{-1} electrolyte flow and 3 mA cm^{-2} current density for BP-S and MP-P, configurations. Inset shows a magnification near $H=0 \text{ T}$.

Figure 10. TEM micrographs of magnetite and distribution size comparison obtained for MP-P configuration at different flows: A) 30 mL min^{-1} , B) 60 mL min^{-1} and C) 90 mL min^{-1} for 3 mA cm^{-2} current density.

Figure 11. TEM micrographs of magnetite in MP-P configuration and histogram comparison obtained at different currents: A) 100 mA, B) 200 mA and C) 300 mA for 30 mL min^{-1} of constant flow.

Figure 12. X-ray diffractograms for nanoparticles obtained with MP-P configuration at different flow and electric current values.

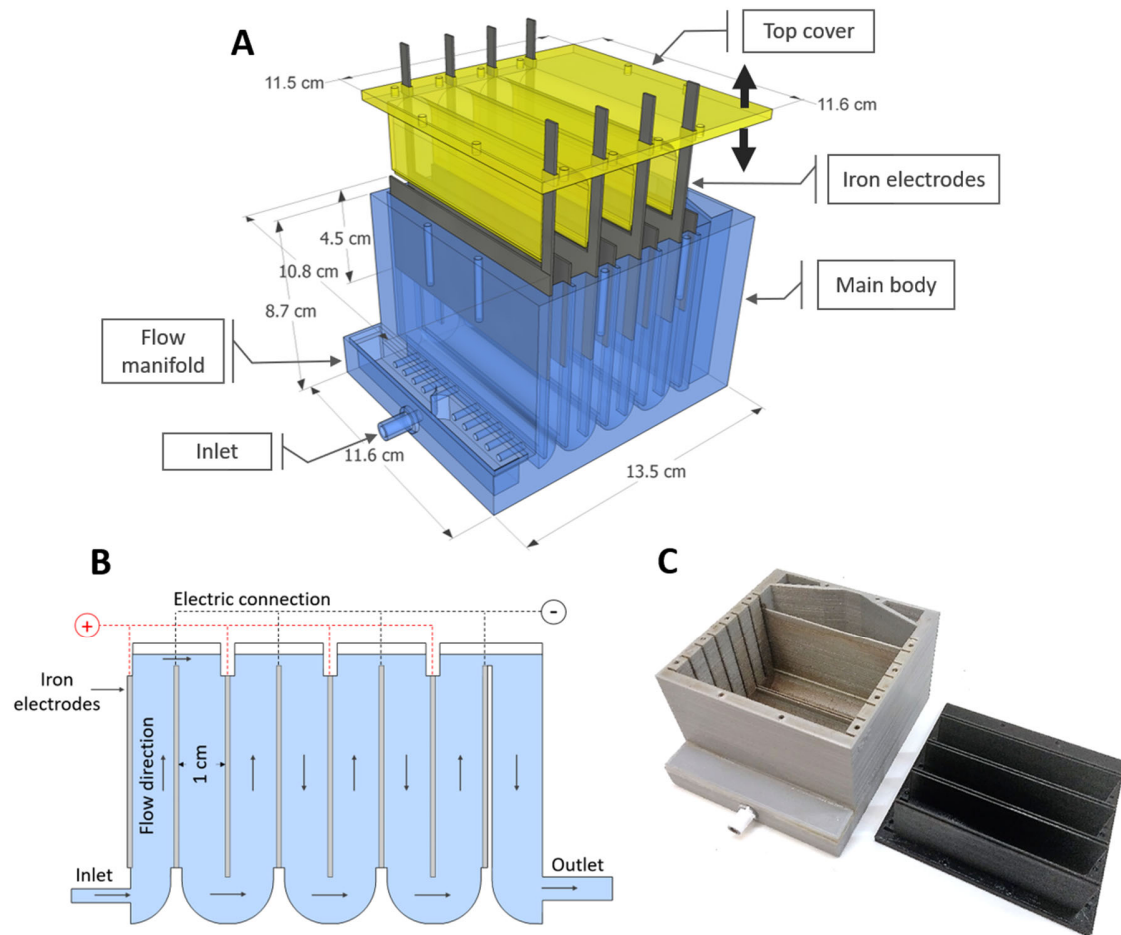


Figure 1

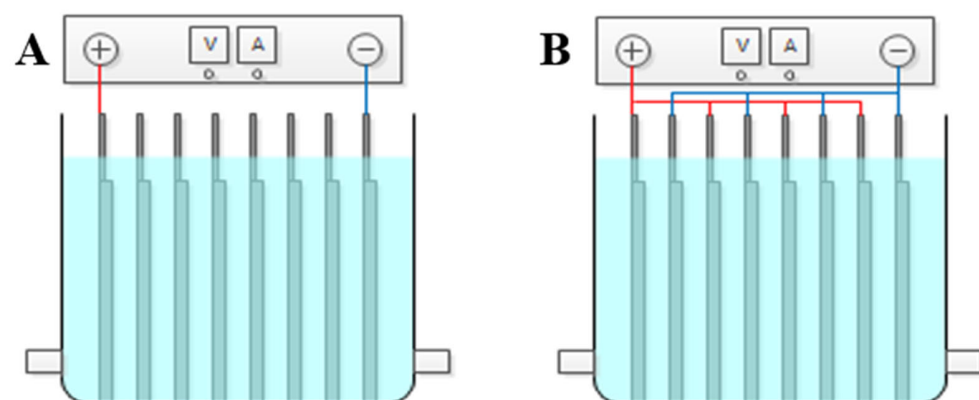


Figure 2

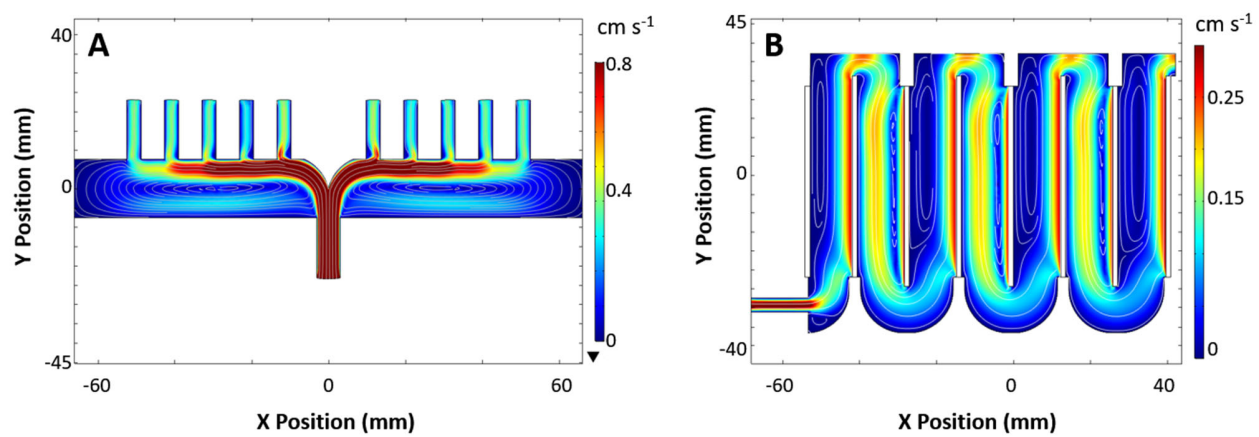


Figure 3

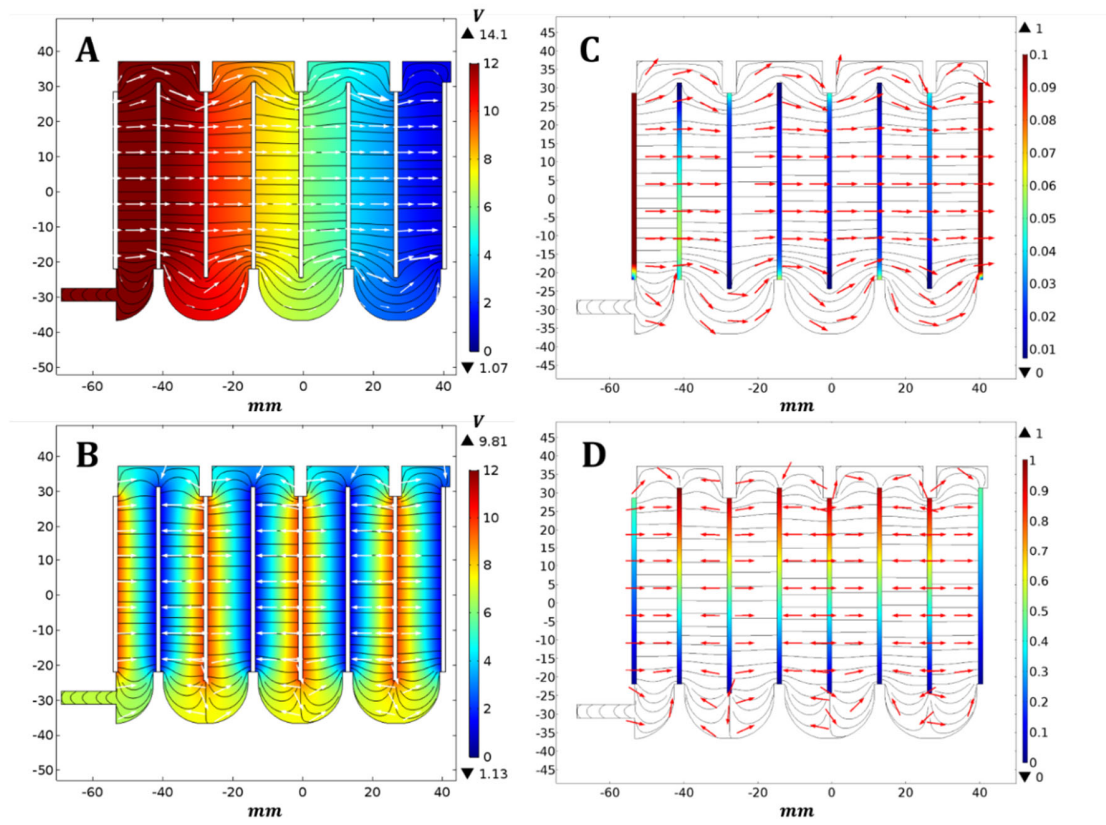


Figure 4

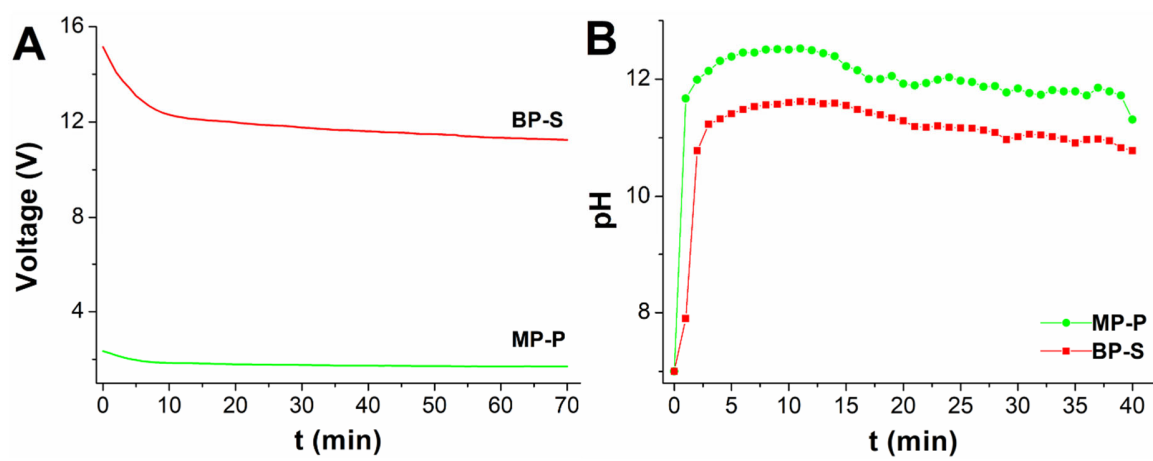


Figure 5

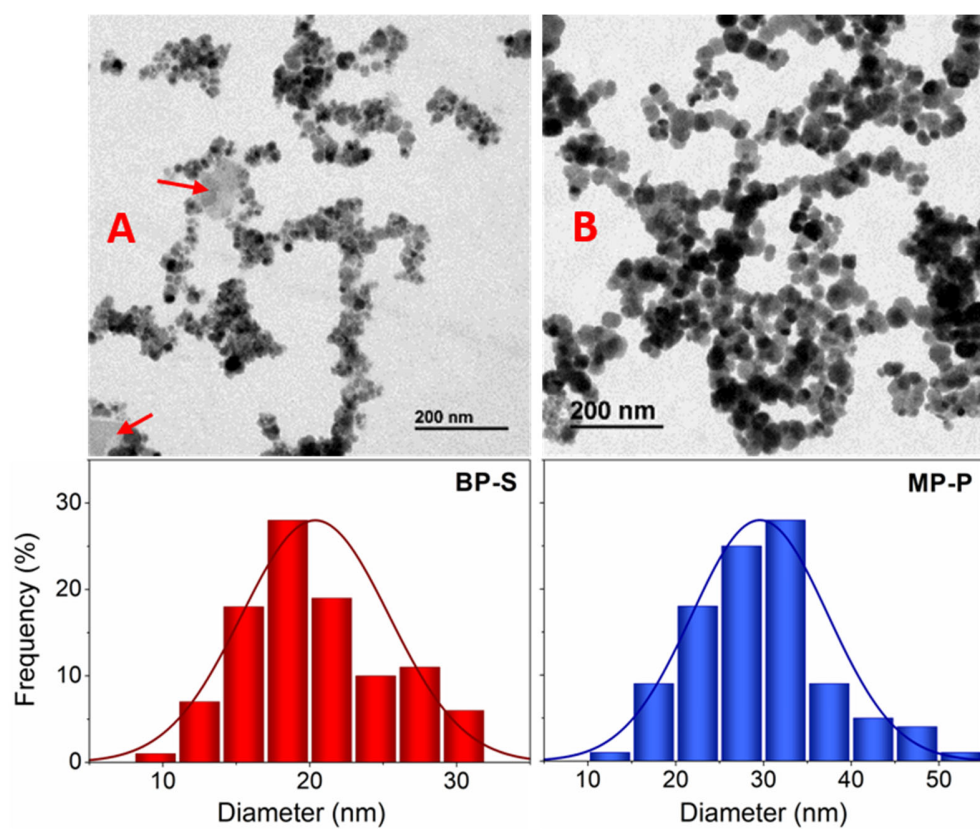


Figure 6

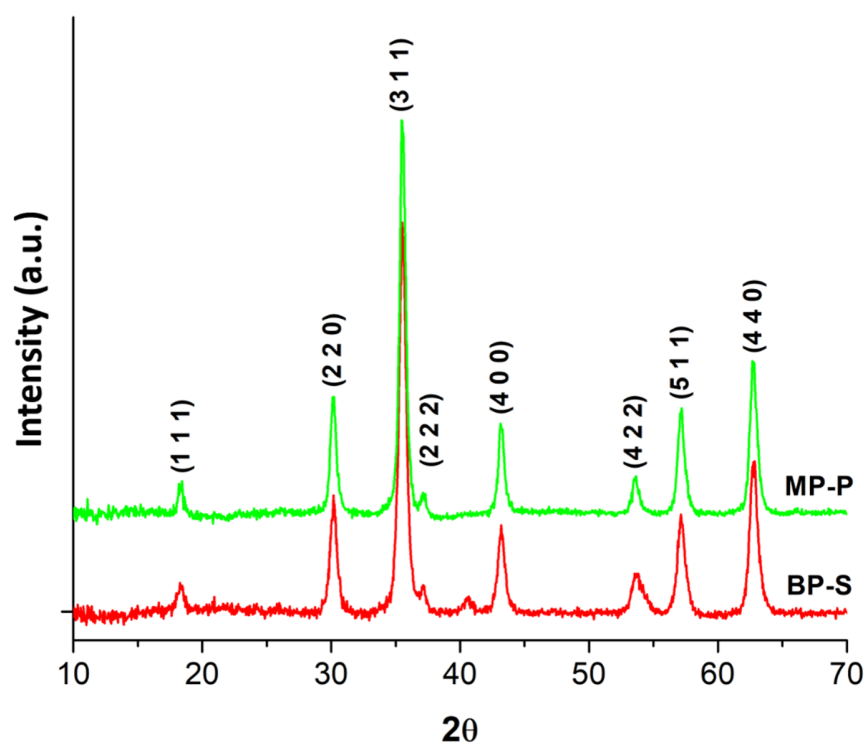


Figure 7

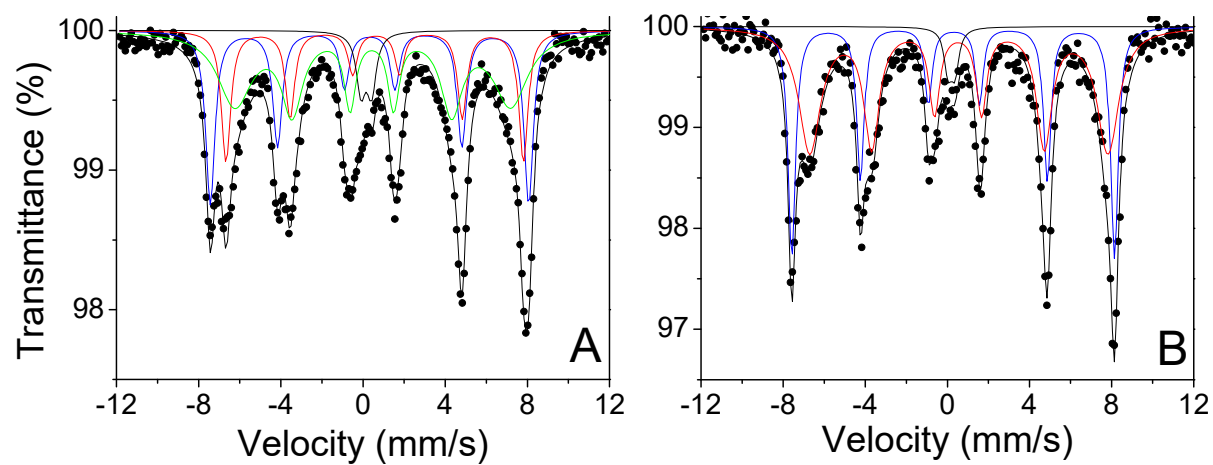


Figure 8

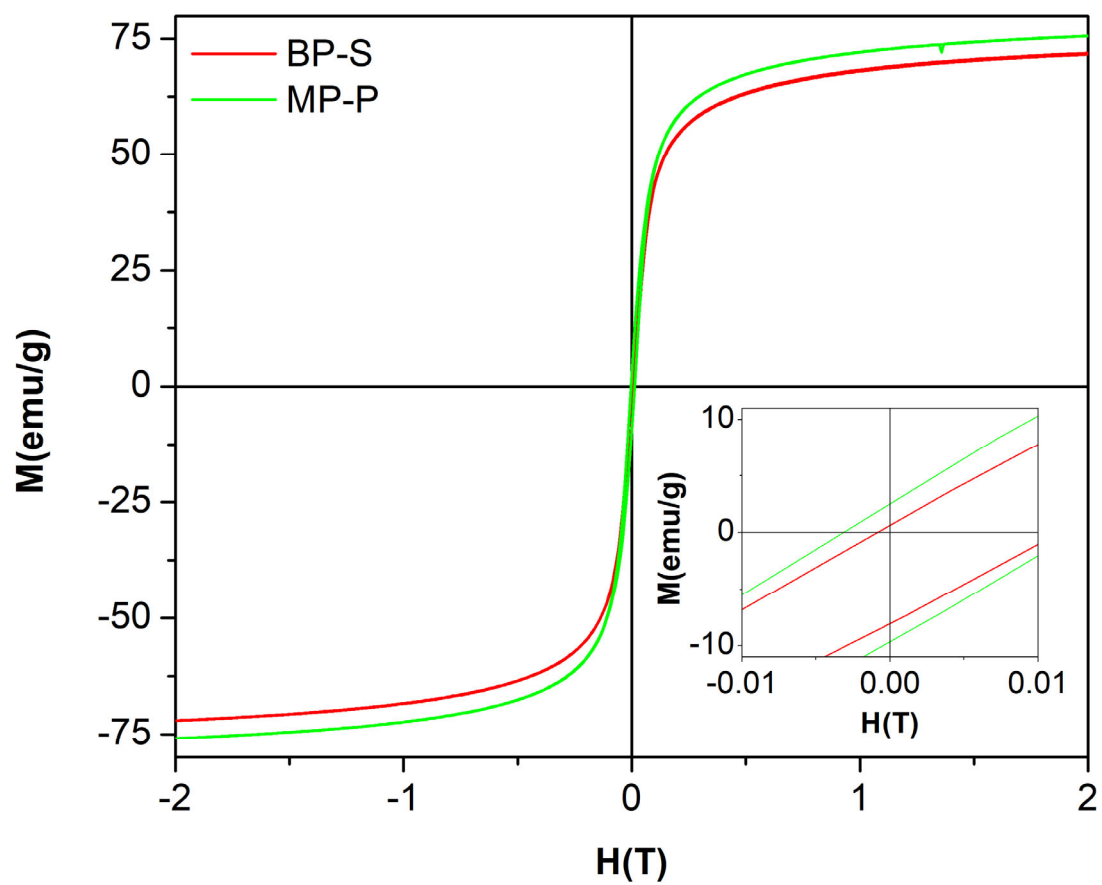


Figure 9

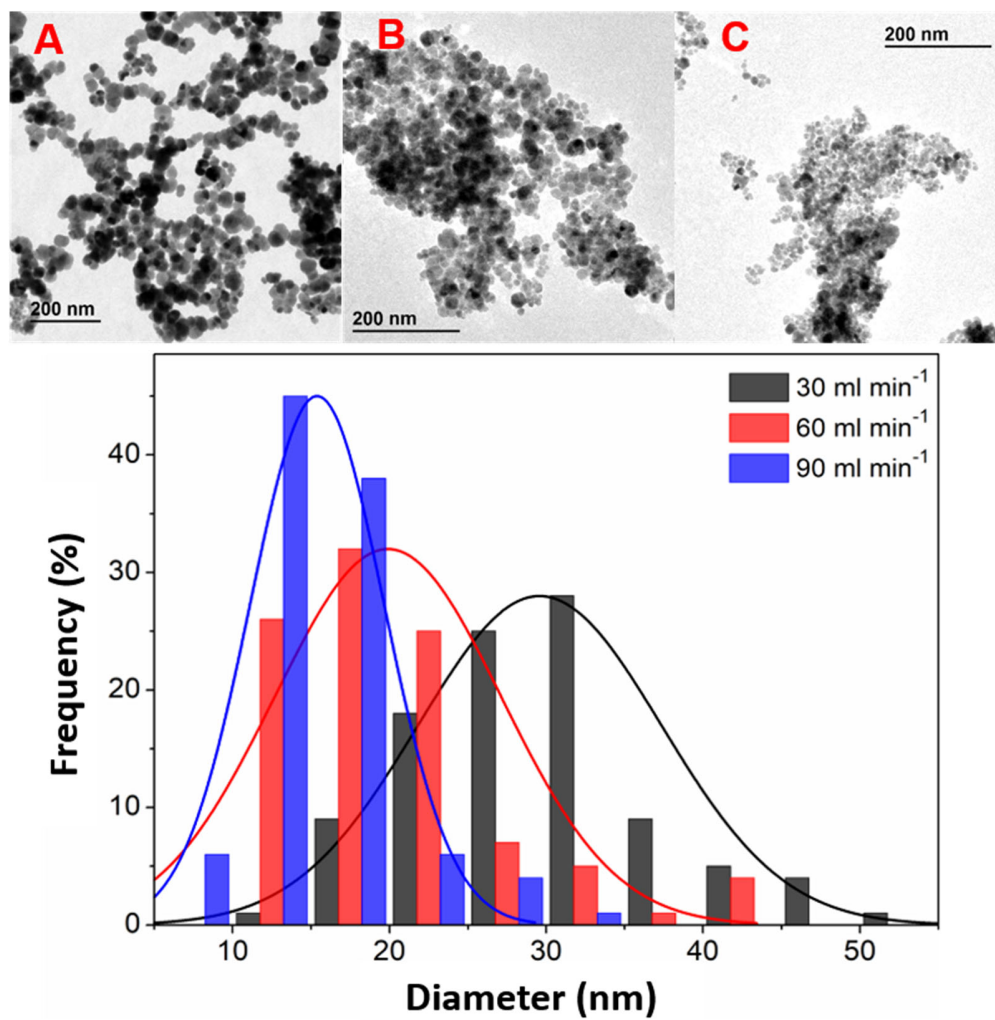


Figure 10

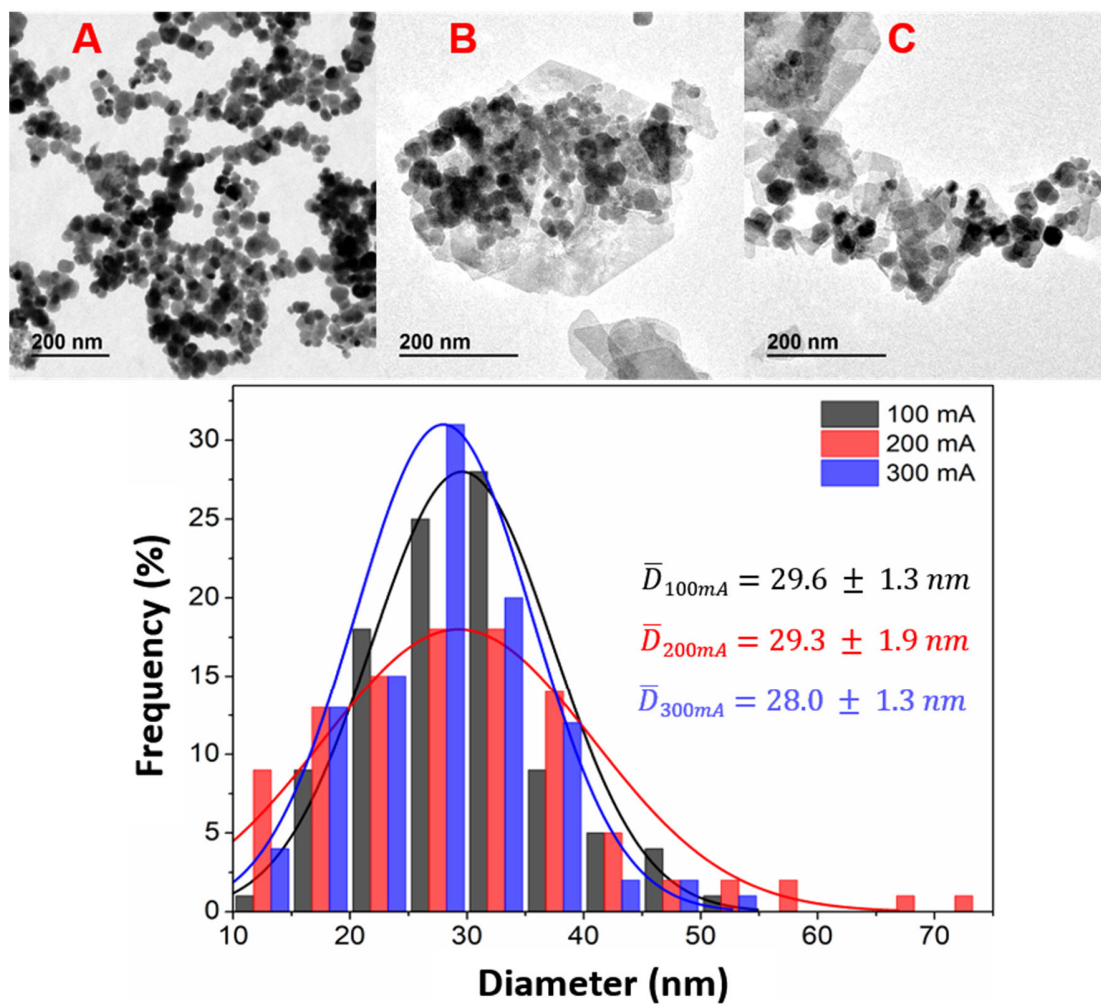


Figure 11

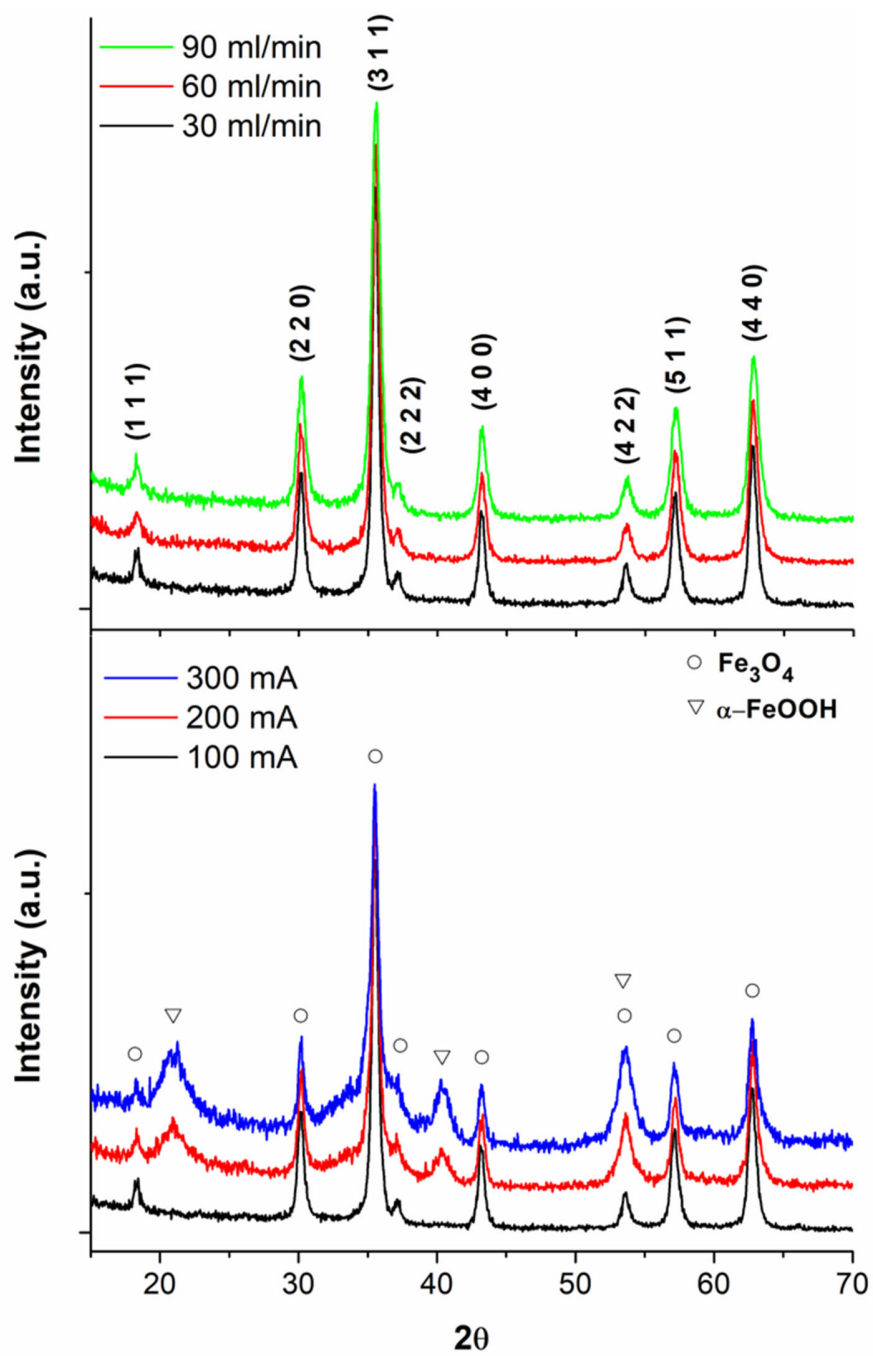


Figure 12

TABLES

Table 1. Parameters and boundary conditions used for FEM flow simulations.

Flow simulation of the inlet manifold			
Laminar flow module			
Section	Parameter	Value	Note
Fluid properties	Density (ρ)	1000 [kg/m ³]	Electrolyte domain
Fluid properties	Dynamic viscosity (μ)	1×10 ⁻³ [Pa s]	Electrolyte domain
Inlet	Flow rate (V_0)	30 [cm ³ /s]	Inlet boundary
Inlet	Entrance length (L_{in})	0.1 [m]	Inlet boundary
Inlet	Entrance thickness (D_z)	5 [mm]	Inlet boundary
Outlet	Exit pressure (p_{out})	1 [atm]	Outlet boundary
Outlet	Exit length (L_{out})	0.02 [m]	Outlet boundary

Flow simulation of the main body			
Laminar flow module			
Section	Parameter	Value	Note
Fluid properties	Density (ρ)	1000 [kg/m ³]	Electrolyte domain
Fluid properties	Dynamic viscosity (μ)	1×10 ⁻³ [Pa s]	Electrolyte domain
Inlet	Average velocity (U_{av})	0.27 [cm/s]	Inlet boundary
Inlet	Entrance length (L_{in})	0.01 [m]	Inlet boundary
Outlet	Pressure (p_{out})	1 [atm]	Outlet boundary
Moving wall	Velocity (u_p)	0.003 [m/s]	H ₂ bubbling

Boundary conditions	
Boundary	Equation
Inlet	$L_{in} \nabla_t \cdot [-p\mathbf{I} + \mu(\nabla_t \mathbf{u} + (\nabla_t \mathbf{u})^T)] = -p_{in} \mathbf{n}$
Outlet	$L_{out} \nabla_t \cdot [-p\mathbf{I} + \mu(\nabla_t \mathbf{u} + (\nabla_t \mathbf{u})^T)] = -p_{out} \mathbf{n}$
Non- slip wall	$\mathbf{u} = \mathbf{0}$
Moving wall	$\mathbf{u} = \mathbf{u}_p^*$
Initial values	$\mathbf{u}_{t=0} = \mathbf{0}$

* velocity field due to hydrogen or oxygen bubbling (approximated from video captures ¹⁵)

Table 2. Parameters and boundary conditions used for FEM current and potential distribution simulations.

Current distribution simulation			
Secondary current distribution module			
Section	Parameter	Value	Note
Electrolyte	Electrolyte conductivity (σ_l)	0.199 [S/m]	Electrolyte domain
Electrode (anodes)	Electrical conductivity (σ_s)	1×10^7 [S/m]	Anode domain
Electrode (cathodes)	Electrical conductivity (σ_s)	1×10^7 [S/m]	Cathode domain
Anode-electrolyte reaction	Equilibrium potential (E_{eq})	-0.44 [V]	Anode boundaries
Anode-electrolyte reaction	Exchange current density (i_0)	100 [A/m ²]	Anode boundaries
Anode-electrolyte reaction	Anodic (α_a) and cathodic (α_c) transfer coefficients	0.5	Anode boundaries
Cathode-electrolyte reaction	Equilibrium potential (E_{eq})	-0.82 [V]	Cathode boundaries
Cathode-electrolyte reaction	Exchange current density (i_0)	1000 [A/m ²]	Cathode boundaries
Cathode-electrolyte reaction	Anodic (α_a) and cathodic (α_c) transfer coefficients	0.5	Cathode boundaries

Boundary conditions

Boundary	Equation
Insulation	$-\mathbf{n} \cdot \mathbf{i}_l = 0 \quad -\mathbf{n} \cdot \mathbf{i}_s = 0$
Electrode reaction	$\eta = \phi_s - \phi_l - E_{eq}$
Electrode current	$I_{s,Total} = 0.1 \text{ A}$
Electric ground	$\phi_s = 0$
Initial values	$\phi_s = 0 \quad \phi_l = 0$

Table 3. Production parameters for BP-S and MP-P configurations.

Configuration	<i>EC</i> (kJ/g)	<i>PR</i> (mg/min)	<i>Ef</i> (%)
BP-S	6.3	3.3	19.4
MP-P	5.9	12.1	72.3

Table 4. Rietveld refinement parameters

Configuration	Crystal size (nm)	Lattice parameter (Å)	Rp	χ^2
BP-S	16.6	8.358	8.94	1.59
MP-P	21.1	8.364	8.64	1.39

Table 5. Summary of magnetic parameters obtained from magnetization curves recorded at 300 K. ($1 \text{ mT} = 0.1 \text{ G}$; $1 \text{ emu/g} = 1 \text{ A m}^2/\text{kg}$)

Configuration	M_s (emu/g)	M_r (emu/g)	M_r/M_s	H_c (mT)
BP-S	73.5	4.33	0.06	0.0079
MP-P	77.3	6.04	0.08	0.0062